Stator-Tooth Optimization of an Induction Machine with Squirrel-Cage Rotor

C. Schlensok, S. Felgenträger, D. van Riesen, and K. Hameyer

Abstract — **Geometry optimization of electric machines allows for a higher efficiency, smoother operational behavior in terms of torque ripple, forces, and vibrations, and beneficial, less cost intensive manufacturing. Usually, permanent-magnet synchronous-machines are subject to geometry optimization. Here, the stator-tooth shape of an induction machine with squirrel-cage rotor is optimized in respect to a reduced peak-to-peak torque ripple and less vibrations providing equal torque as the non-optimized machine.**

Index Terms — **FEM, induction machine, geometry optimization, vibrations, structure dynamics, acoustics.**

I. Introduction

GEOMETRY optimization for cogging torque reduction is a well known technique concerning permanent-magnet synchronous-machines, linear actuators, transformers, and chip design. [1-8] show just some selected examples. For Induction Machines with squirrel-cage rotor (IM) geometry optimization, i.e. tooth shape optimization, is a new field. Here, the focus is on the reduction of the torque-ripple and the noise radiation providing the same average torque compared to standard IMs.

For the optimization the Finite-Element Method (FEM) is applied. A transient solver [9] is used for the simulation of the flux-density distribution in the IM. Transient simulation requires a high number of time steps for the transient phenomenon of the magnetic field. After this has died out the magnetic field values and its derivates such as torque and forces can be analyzed. Therefore, the geometry optimization of an IM results in a much higher effort and a cost intensive process in terms of computing time than in the case of time-independent or non-transient behaving electromagnetic devices.

Due to the high computing costs the optimization process is divided into two serial and iterated steps as Fig. 1 shows. In the first step the shape of the stator teeth is modified and the IM is simulated electromagnetically. The torque is calculated. In the case of an improvement of the torque ripple a structure-dynamic simulation is performed to simulate the vibrations and the body sound of the IM in a second step. These two steps are repeated until there is no significant variation in the results.

II. Shape Optimization

The torque ripple depends on the permittivity function of the air gap which corresponds to the teeth shape of both stator and rotor [10]. The tips of the rotor teeth cannot be changed. The manufacturing of the squirrel-cage rotor does not allow for this. Therefore, only the shape of the stator teeth can be modified and optimized. Each edge of the ferromagnetic lamination leads to flux concentration and therefore high flux density values in these regions. These result in an oscillation of the torque, i.e. torque ripples. Hence, the tooth tips have to be smoothed for low torque ripple.

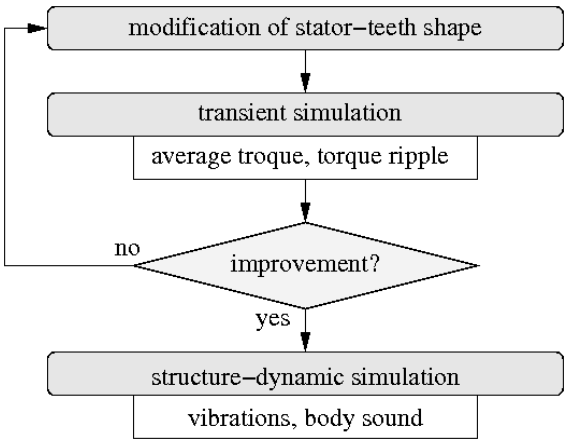

Fig. 1. Flow chart of the optimization process.

The shape modification applying the FEM is performed in three steps. At first the nodes of the stator-teeth mesh at the air gap of the FE-model are re-located by moving them in radial direction and the mesh is adopted (Fig. 2). Then the transient electromagnetic FEM-simulation is performed resulting in the flux-density distribution from which the time-dependent torque behavior is derived. Depending on the torque-ripple and the average torque the nodes of the stator teeth are then re-located and the simulation loop is repeated.

At first a FE-model of the reference geometry (Fig. 3) is simulated considering the skewing of the rotor slots by applying the multi-slice method [11]. Then the nodes of the stator teeth are re-located moving the outer nodes "faster" than the inner and keeping the central node fixed (node no. 9 in Fig. 2). The modified models and a reference model for comparison are simulated both without any skewing.

III. Torque-Ripple Optimization

The modification of the tooth shape (model $\Delta T_{\min.}$, Fig. 4) results in a very small torque ripple as Fig. 5 and 6 show. The non-skewed reference model has the highest average torque but also the highest torque ripple, which is about 176.2 % higher than in the case of the model with a skewed rotor (Fig. 6). The reduction in the case of the first optimized model

Manuscript received July 15th, 2006.

C. Schlensok, S. Felgenträger, D. van Riesen, and K. Hameyer are with the Institute of Electrical Machines, RWTH Aachen University, D-52056 Aachen, Germany. (phone: +49-241-8097667; fax: +49-241-8092270; e-mail: Christoph.Schlensok@ iem.rwth-aachen.de).

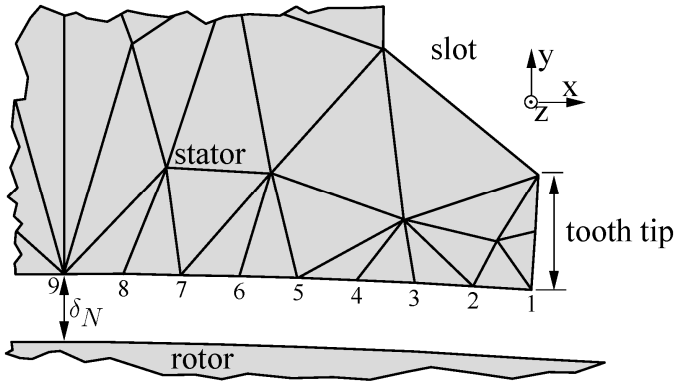

Fig. 2. Re-location of stator-teeth nodes, detail region.

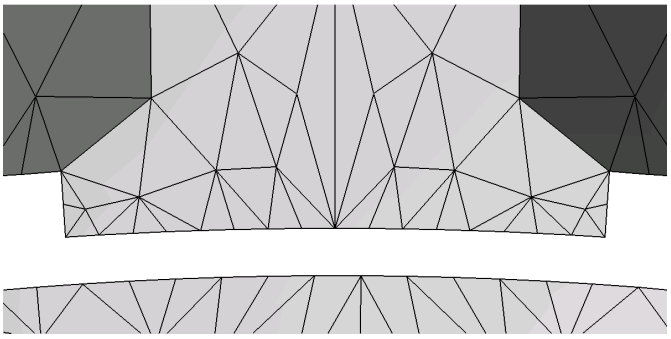

Fig. 3. Stator-tooth shape of reference model.

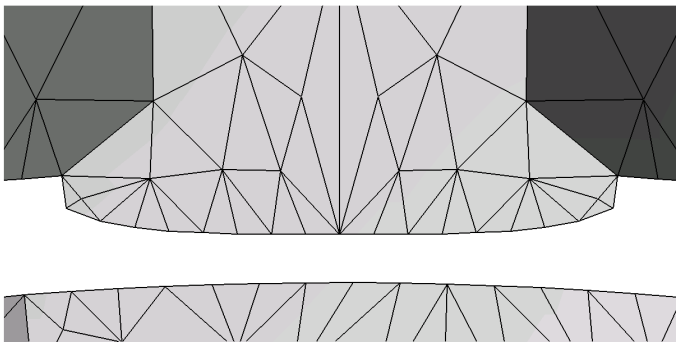

Fig. 4. Stator-tooth shape of model with minimized torque ripple.

compared to the non-skewed reference model is 71.5 %. This is by far lower than a skewed motor with original tooth-shape design (-49.8 %). On the other hand the average torque decreases to 94.5 % of the reference torque. This loss of torque is unacceptable. Therefore, the new shape is again optimized now taking the average torque as parameter into respect.

The second optimization results is a shape having a concave tooth in the center region comparable to the reference tooth and smooth tool tips as the tooth of the model with low torque ripple has (Fig. 7). This tooth shape results in a smaller average air gap as model $\Delta T_{\min}$. Therefore, the average torque is 96.8 % of the reference torque (non-skewed model) and 103.7 % compared to a skewed motor. The torque ripple is reduced by 63.9 % when compared to the non-skewed and by 36.3 % taking the skewed motor into account. Therefore, the last modified model is taken as "optimized" model. In the following this model is taken into consideration.

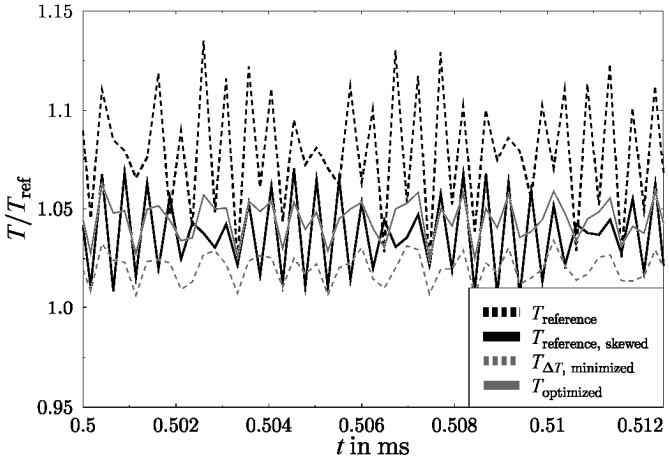

Fig. 5. Time-dependent torque behavior.

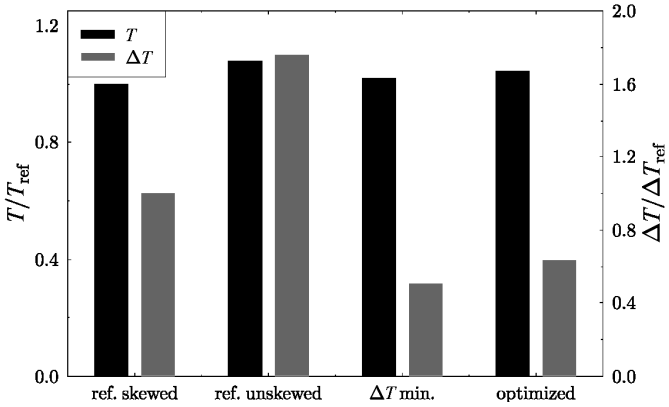

Fig. 6. Average torque and torque ripple.

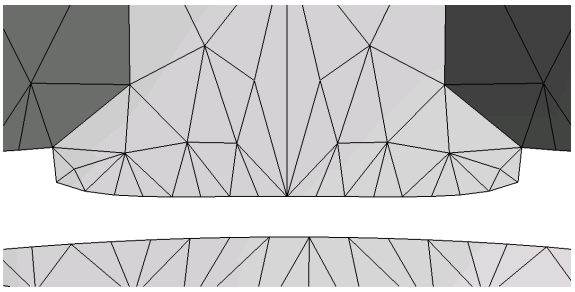

Fig. 7. Stator-tooth shape of model with low torque ripple and high average torque.

IV. Analysis of the Surface-Force Density

The electromagnetic simulation is performed in a transient manner in the time domain. Therefore, the surface-force density σ on the border of the stator teeth used for the succeeding structure-dynamic simulation is also calculated in the time domain. For each simulation-time step σ is derived from the flux-density distribution applying the Maxwell's-stress tensor-method [14,15]. Fig. 8 depicts the force distribution for one single simulation time step and one stator tooth of the reference model. Since the rotor is revolving counter-clock wise, the maximum forces are reached on the up-running edges of the stator teeth, here, the right tooth tip.

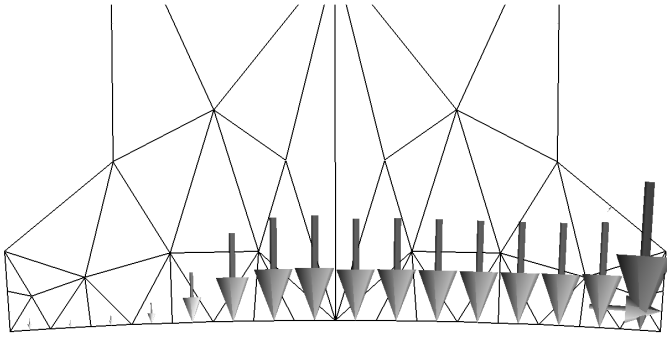

Fig. 8. Surface-force density-distribution on the border of the reference model for one single simulation-time step.

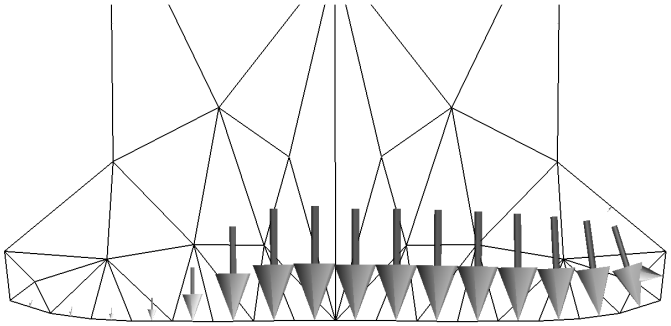

Fig. 9. Surface-force density-distribution on the border of the optimized model for one single simulation-time step.

When comparing the force excitation of the same simulation-time step for the optimized stator-tooth shape the maximal forces are no longer located on the tooth tips (Fig. 9). Due to the larger air gap in this region the flux density is reduced significantly. The tooth is excited more uniformly.

The surface-force density is transformed to frequency domain for both models. From the resulting spectrum, measurements, and the analytic theory of [12] the frequencies for structure-dynamic analysis are selected. Table I sums them up for the regarded point of operation at a rotor speed of n = 1200 min^{-1} and a stator frequency of f_1 = 48.96 Hz.

Table. I. Selected frequencies from the surface-force density-spectrum.

f [Hz]	98	422	520	618
f [Hz]	716	942	1040	1138

V. Body-Sound Analysis

For the selected frequencies of the surface-force density derived from Table I a structure-dynamic simulation is performed [13]. Fig. 10 shows the mechanical FE-model used for the structure-dynamic simulation. It consists of all mechanical parts, such as the rotor, with the short-circuit rings and the shaft, the stator including the winding and the winding heads, the end shields, the bearings, and the housing which is coupled to the stator with six spiral-steel springs. The model is simulated with a displacement solver developed at the Institute of Electrical Machines at RWTH Aachen University [16]. The simulation model provides the deformation for each of the 27.215 nodes of the FE-model for the selected frequencies from Table I.

In three different ways the deformation of the machine is analyzed:

1. Analysis of the deviation of the deformation between the reference model and the optimized IM,
2. Analysis of the body-sound level L_S, which is calculated at a predefined location allowing comparison with measurements,
3. And the analysis of the body-sound index L_{BSI} taking the complete deformation of an entire body, e.g. the housing, into account.

These methods allow for a detailed comparison of various force excitations of the stator teeth due to e.g. variants of the stator-tooth shape.

A. Deviation of the deformation

Fig. 11 and 12 show the deviation of the deformation of the housing and the stator for the two selected frequencies f = 942 and 1040 Hz. The two figures show exemplarily the non-uniform impact of the optimized stator-tooth shape in comparison to the reference model on the IM's deformation. At f = 942 Hz (Fig. 11) the optimized tooth shape results in higher deformation throughout the stator and the housing as the dominating dark colors indicate. A similar result can be stated for f = 422 Hz. In the case of f = 1040 Hz (Fig. 12) the contrary behavior occurs. Especially the stator region is less deformed. Similar results are found for f = 520, 618, and 1138 Hz.

B. Body-sound level

The body-sound level L_S is calculated along two lines on both ends of the housing (Fig. 13). Since the IM is mounted on the A-side the B-side can oscillate more freely. Along the

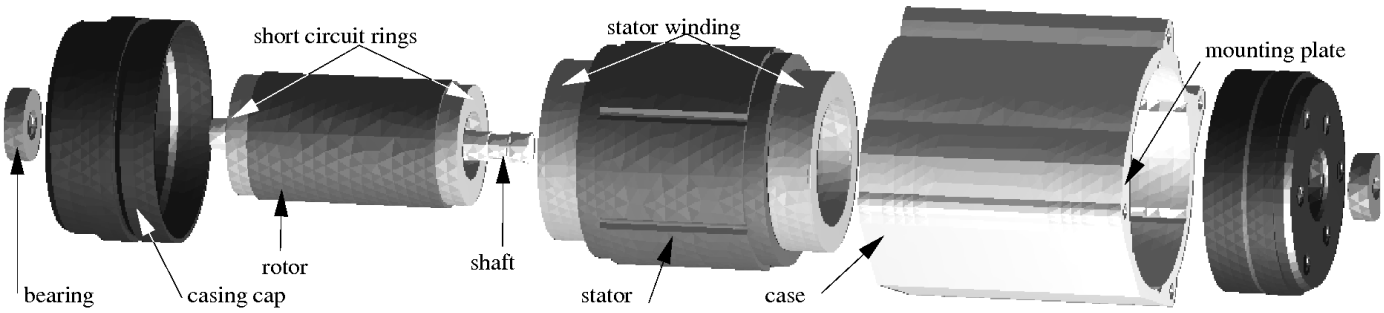

Fig. 10. Mechanical FE-model for the structure-dynamic simulation (exploded view).

sampling lines the deformation of the housing is sampled and transformed into the complex-valued acceleration $\underline{a}$ of these points in local cylinder coordinates and depending on the studied frequency $\omega = 2\pi f$:

$$\vec{\underline{a}} = -\omega^2 \cdot \vec{\underline{u}}_{\text{local}} \ . \tag{1}$$

The local coordinates depend on the location of the sampling point on the housing:

$$\vec{\underline{u}}_{local} = \begin{pmatrix} \underline{x} \cdot \vec{e}_x \cdot \vec{e}_{rad} + \underline{y} \cdot \vec{e}_y \cdot \vec{e}_{rad} + \underline{z} \cdot \vec{e}_z \cdot \vec{e}_{rad} \\ \underline{x} \cdot \vec{e}_x \cdot \vec{e}_{\tan} + \underline{y} \cdot \vec{e}_y \cdot \vec{e}_{\tan} + \underline{z} \cdot \vec{e}_z \cdot \vec{e}_{\tan} \\ \underline{x} \cdot \vec{e}_x \cdot \vec{e}_{ax} + \underline{y} \cdot \vec{e}_y \cdot \vec{e}_{ax} + \underline{z} \cdot \vec{e}_z \cdot \vec{e}_{ax} \end{pmatrix} . \tag{2}$$

With this L_S is calculated by

$$L_S = 20 \cdot \log \frac{|\underline{a}|}{a_{ref}} \text{dB} \ . \tag{3}$$

Where $a_{ref} = 1\ \mu\text{m/s}^2$ is a reference value.

Fig. 14 depicts the radial component of the deformation along the sampling lines. As can be seen the deformation of the housing is lower but shows higher oscillation on the A-side. The minimums represent the four drilling holes for the mounting which are fixed in the simulation. The maximums show the regions close to the six spiral springs where the vibration of the stator are transmitted to the housing. On the B-side the deformation is more uniform but still showing the described mechanical configuration.

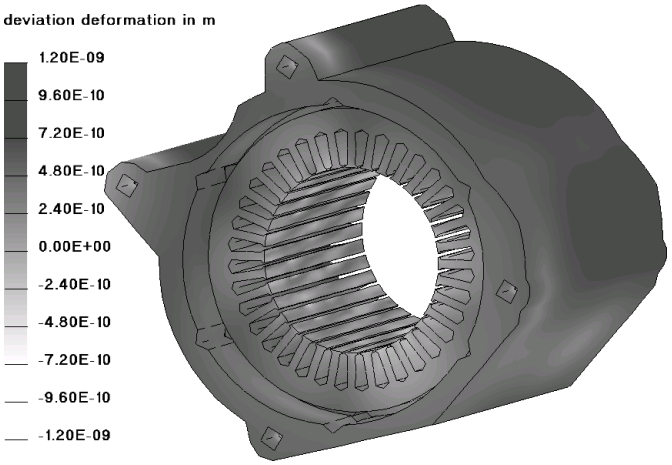

Fig. 11. Deviation of deformation between reference and optimized tooth shape: $f = 942$ Hz.

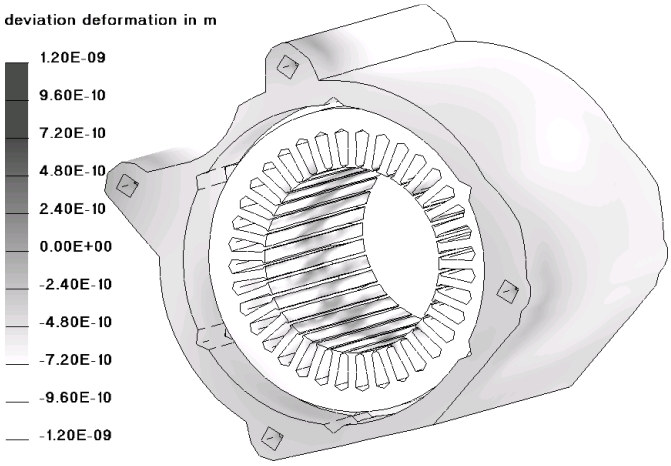

Fig. 12. Deviation of deformation between reference and optimized tooth shape: $f = 1040$ Hz.

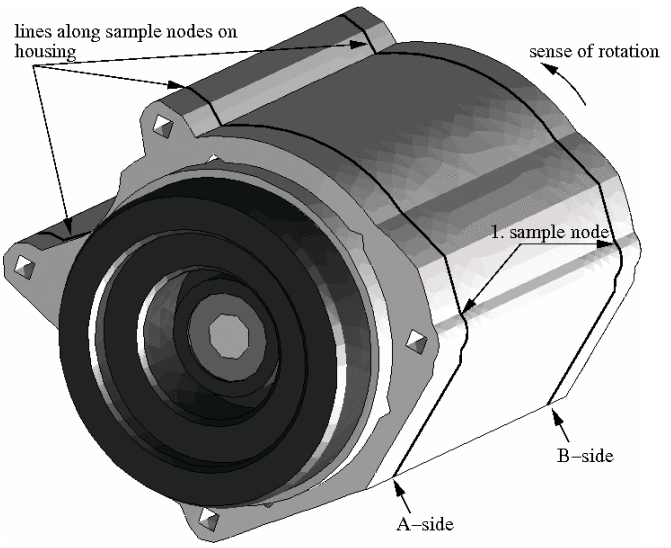

Fig. 13. Sampling lines for the calculation of the body-sound level L_S.

The sampled values of the deformation are averaged to create a more general criteria. Fig. 15 and 16 show the results for the radial and axial components on both sides of the IM for all selected and simulated frequencies. The values of the reference model are subtracted from the values from the optimized model.

The levels on the mounted A-side show slightly lower deviation as on the B-side. For the radial and the tangential component the behavior is the same in general. Therefore, only the radial component is depicted. For this the stator-tooth shape-optimization results in significantly higher deformation

C. Body-sound index

Finally, the body-sound index L_{BSI} is analyzed. In contrast to the L_S the L_{BSI} allows for the analysis of the deformation of an

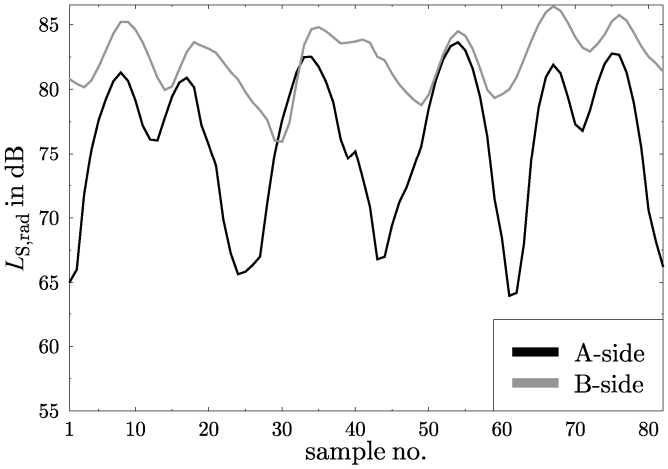

Fig. 14. Deformation along the sampling lines for $f = 422$ Hz.

entire body, e.g. the housing of the IM. The deformation of the body is integrated and is related to a reference value:

$$L_S(f) = 10 \cdot \log\left(\frac{\sum_{p=1}^{N} f \left| \underline{u}_p \cdot \mathbf{n}^p \right|^2 dS}{S_0 \cdot h_{U_0}^2} \right). \quad (4)$$

With $\mathbf{n}^p$ being the normal vector on the p^{th} element. up is the deformation of the corresponding element, N the number of elements and $S_0 = 1$ m^2 and $h_{U0}{}^2 = 25\ 10^{-16}$ m^2/s^2 are the reference values.

Fig. 17 shows the results of the L_{BSI} and Fig. 18 the deviation between the optimized and the reference model. The highest overall value is reached for both models at $f = 720$ Hz. In the case of the optimized model the L_{BSI} increases for $f = 422$ and 942 Hz. For $f = 1040$ and 1138 Hz the levels are reduced significantly.

Taking all analysis criteria into account the optimized model shows an improved behavior in general with the exception of $f = 422$ and 942 Hz.

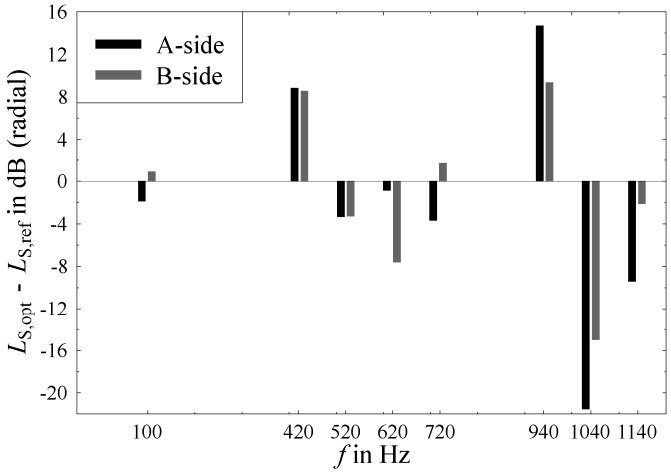

Fig. 15. Radial component of the deviation of the L_S.

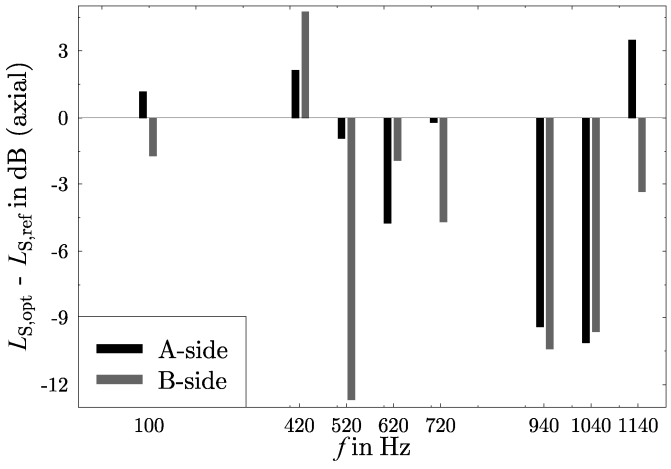

Fig. 16. Axial component of the deviation of the L_S.

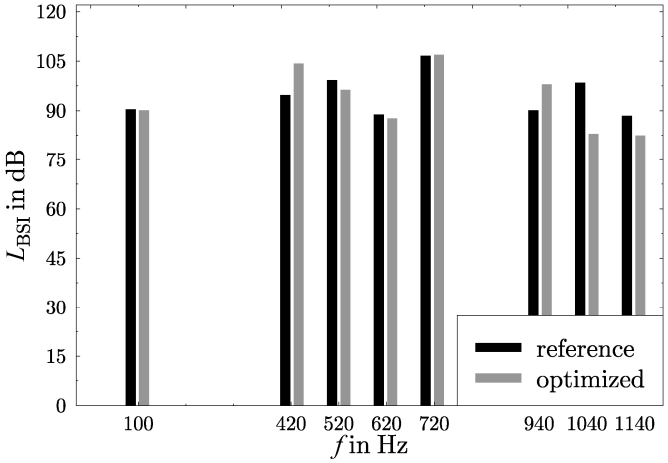

Fig. 17. L_{BSI} for both models.

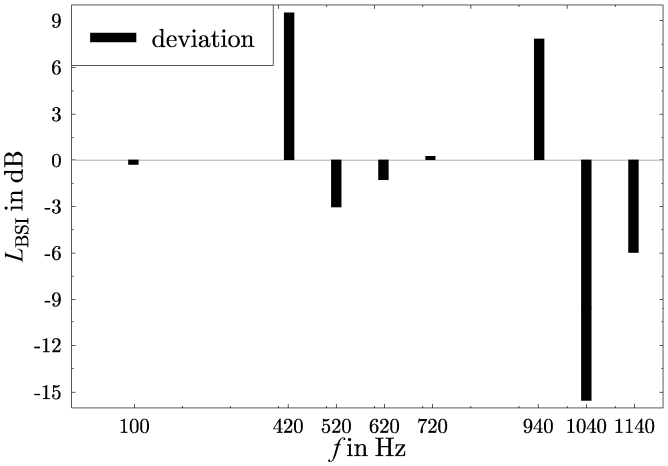

Fig. 18. Deviation of the L_{BSI} between both models.

VI. Conclusions

In this paper the geometry optimization of an Induction Machine with squirrel-cage rotor (IM) is presented. The stator-tooth shape is modified in such a way, that the torque ripple is reduced significantly without losing torque at the same time. The resulting tooth shape show smoothened edges and a concave center part. The smooth edges reduce the torque ripple and high local electromagnetic surface forces. Both the torque ripple and the forces are by far lower than in the case of a skewed IM. The concave center part allows for similar values for the load torque when compared to a skewed IM. Table II resumes these results. The optimized tooth shape allows for a non-skewed rotor. Such an IM has a higher load torque and a smaller torque ripple.

Table. II. Selected Resume of torque and torque ripple values.

model	relative torque	relative ripple
non-skewed	1.00	1.00
skewed	0.93	0.57
ripple minimized	0.95	0.28
optimized	0.97	0.36

In a second analysis step the deformation of the IM is simulated considering the surface-force density from the electromagnetic models of the non-skewed reference model and the optimized stator-tooth shape-model. The results of these structure dynamic simulations show non-uniform tendencies. For f = 422 and 942 Hz the optimized stator-tooth shape results in significantly higher body sound. Nevertheless, the deformation is reduced for the other studied frequencies.

The applied optimization method and the presented results of both the electromagnetic and structure-dynamic simulations imply that the optimization of the stator-tooth geometry of an IM is reasonable and allows for an significant improvement of the IM's performance. More even, the optimized shape allows for a non-skewed rotor. Hence, the manufacturing of the optimized IM is less cost intensive.

REFERENCES

[1] M.A. Tsili, A.G. Kladas, P.S. Georgilakis, A. T. Souflaris, D. G. Paparigas, "Geometry optimization of magnetic shunts in power transformers based on a particular hybrid finite-element boundary-element model and sensitivity analysis," *IEEE Trans. on Magn.*, vol 41, no. 5, pp. 1776 – 1779, May 2005.

[2] M.F. Reusch, D.W. Weissenburger, J.C.Nearing, "Optimization of magnet end-winding geometry," *IEEE Trans. on Magn.*, vol 30, no. 2, pp. 162 - 167, March 1994.

[3] K. Le Phan, H. Boeve, F. Vanhelmont, T. Ikkink, W. Talen, "Geometry optimization of TMR current sensors for on-chip IC testing," *IEEE Trans. on Magn.*, vol 41, no. 10, pp. 3685 - 3687, October 2005.

[4] L. Hadjout, N. Takorabet, R. Ibtiouen, S. Mezani, "Optimization of Instantaneous Torque Shape of PM Motors Using Artificial Neural Networks Based on FE Results," *IEEE Trans. on Magn.*, vol 42, no. 4, pp. 1283 - 1286, April 2006.

[5] L. Wang, D. A. Lowther, "Selection of Approximation Models for Electromagnetic Device Optimization," *IEEE Trans. on Magn.*, vol 42, no. 4, pp. 1227 - 1230, April 2006.

[6] E. Dilettoso, N. Salerno, "A Self-Adaptive Niching Genetic Algorithm for Multimodal Optimization of Electromagnetic Devices," *IEEE Trans. on Magn.*, vol 42, no. 4, pp. 1203 - 1206, April 2006.

[7] D. Echeverria, D. Lahaye, L. Encica, E. A. Lomonova, P. W. Hemker, A. J. A. Vandenput, "Manifold-Mapping Optimization Applied to Linear Actuator Design," *IEEE Trans. on Magn.*, vol 42, no. 4, pp. 1183 - 1186, April 2006.

[8] Y. Yang, X. Wang, R. Zhang, T. Ding, R. Tang, "Manifold-Mapping Optimization Applied to Linear Actuator Design," *IEEE Trans. on Magn.*, vol 42, no. 4, pp. 1135 - 1138, April 2006.

[9] D. van Riesen, C. Monzel, C. Kaehler, C. Schlensok, G. Henneberger, "iMOOSE-an open-source environment for finite-element calculations," *IEEE Trans. on Magn.*, vol 40, no. 2, pp. 1390 - 1393, March 2004.

[10] S.-M. Hwang, J.-B. Eom, Y.-H. Jung, D.-W. Lee, B.-S. Kang, "Various design techniques to reduce cogging torque by controlling energy variation in permanent magnet motors," *IEEE Trans. on Magn.*, vol 37, no. 4, pp. 2806 - 2809, July 2001.

[11] J. J. C. Gyselinck, L. Vandevelde, J. A. A. Melkebeek, "Multi-slice FE modeling of electrical machines with skewed slots – the skew discretization error," *IEEE Trans. on Magn.*, vol 37, no. 5, pp. 3233 - 3237, September 2001.

[12] H. Jordan, *Geräuscharme Elektromotoren*, Verlag W. Giradet, Essen, 1950.

[13] C. Schlensok, D. van Riesen, T. Küest, G. Henneberger, "Acoustic calculation of an induction machine with squirrel-cage rotor," *COMPEL*, vol. 25, no. 2, pp 475-486, April 2006.

[14] O. C. Zienkiewicz, R. L. Taylor, *The finite element method*, McGraw-Hill Book Company, London, 1989.

[15] J. P. A. Bastos, N. Sadowski, *Electromagnetic modeling by finite element methods*, Marcel Dekker, Inc., New York, Basel, 2003.

[16] D. van Riesen, C. Monzel, C. Kaehler, C. Schlensok and G. Henneberger, " iMOOSE - An Open-Source Environment for Finite-Element Calculations," , *IEEE Trans. on Magn.*, vol 40, no. 2, pp. 1390 - 1393, March 2004.